

Giant ZT enhancement in rhombohedral GeTe-based thermoelectric materials

Received: 25 December 2025

Accepted: 3 March 2026

Published online: 15 March 2026

 Check for updates

Jincheng Yu^{1,10}, Xiaodong Liu^{2,10}, Yilin Jiang^{3,10} ✉, Chen Chen³,
Jing-Wei Li⁴, Haihua Hu⁵, Lin Song⁶, Tian Xie⁷, Bin-Bin Ruan¹, Yu Pan⁷ ✉,
Guoyu Wang⁷, B. Layla Mehdi^{2,8}, Xiaoyuan Zhou¹ ✉ & Jing-Feng Li^{3,9} ✉

The peak figure of merit (ZT) of GeTe-based thermoelectric (TE) materials is typically attained in the high-temperature cubic phase, where the inevitable phase transition raises concerns over interfacial instability during operation. Therefore, developing high-performance rhombohedral GeTe below the phase transition temperature represents a more viable path toward practical applications. Herein, we propose a facile nanocomposite strategy to enhance the TE performance of rhombohedral GeTe by incorporating high-modulus TiB_2 nanoparticles into $\text{Ge}_{0.94}\text{Bi}_{0.05}\text{Te}$ matrix. We demonstrate that the nanoparticle-induced interfacial constraint effect contributes to increasing longitudinal elastic modulus and decreasing equivalent deformation potential, accounting for improved carrier mobility. Additionally, these TiB_2 inclusions form heterogeneous interfaces that promote charge depletion and generate substantial thermal resistance, concurrently suppressing the heat transfer by carriers and phonons. Consequently, an extraordinary ZT of 2.66 at 613 K and a superior average ZT of 1.29 (300 ~ 613 K) are obtained in the rhombohedral GeTe-based composite. This work shows a paradigm for synergistically optimizing the electrical and thermal transports of emerging TE systems with nano-inclusions.

By enabling direct solid-state conversion between heat and electricity, thermoelectric (TE) materials offer an alternative pathway for power generation and refrigeration, holding considerable promise for advancing waste heat recovery and thermal management solutions¹. The conversion efficiency of TE materials is typically characterized by the dimensionless figure of merit, $ZT = S^2\sigma T / (\kappa_e + \kappa_L)$, where S is the Seebeck coefficient, σ is the electrical conductivity, T is the absolute temperature, κ_e is the electronic thermal conductivity, and κ_L is the lattice thermal conductivity². Therefore, the key to improving the

thermoelectric performance lies in maximizing the power factor ($PF = S^2\sigma$) or minimizing the thermal conductivity ($\kappa = \kappa_e + \kappa_L$) to endow the candidate materials with the characteristics of electron crystal-phonon glass³.

Despite being the most successful commercial TE material to date, Bi_2Te_3 operates primarily within a near-ambient temperature range⁴, which limits its use for broader, more diverse applications. By contrast, GeTe presents itself as a promising TE material for sustained service within the mid- and high-temperature range⁵. Not only does it

¹College of Physics and Center of Quantum Materials & Devices, Chongqing University, Chongqing, China. ²Department of Materials, Design & Manufacturing Engineering, University of Liverpool, Liverpool, UK. ³State Key Laboratory of New Ceramic Materials, School of Materials Science and Engineering, Tsinghua University, Beijing, China. ⁴State Development and Investment Corporation, Beijing, China. ⁵Max Planck Institute for Chemical Physics of Solids, Nöthnitzer Str. 40, Dresden, Germany. ⁶School of Mechanical Engineering, Shandong University, Jinan, China. ⁷College of Materials Science and Engineering and Center of Quantum Materials & Devices, Chongqing University, Chongqing, China. ⁸Albert Crewe Centre, University of Liverpool, Liverpool, UK. ⁹Department of Applied Physics, Graduate School of Engineering, Tohoku University, Sendai, Japan. ¹⁰These authors contributed equally: Jincheng Yu, Xiaodong Liu, and Yilin Jiang. ✉ e-mail: jyL_materials@163.com; yupan2024@cqu.edu.cn; xiaoyuan2013@cqu.edu.cn; jingfeng@mail.tsinghua.edu.cn

offer an eco-friendly profile by being lead-free, a notable advantage over high-performance PbTe⁶, but also delivers outstanding *ZT* values mainly due to its good electrical transport (e.g., *PF* can reach over 40 $\mu\text{Wcm}^{-1}\text{K}^{-2}$ at 673 K⁷) in spite of intrinsically high thermal conductivity (e.g., κ exceeds 7 $\text{Wm}^{-1}\text{K}^{-1}$ at room temperature⁸).

Nevertheless, the practical application of GeTe thermoelectrics still faces several challenges. On one hand, the maximum *ZT* value is usually attained in cubic GeTe (over 615 K); the inherent phase transition from low-temperature rhombohedral to high-temperature cubic structure calls for the implementation of segmented architectures in TE devices^{9,10}, raising additional concerns over interfacial instability. On the other hand, the TE performance of GeTe within the temperature range of 300–615 K awaits further optimization, because the abundant intrinsic Ge vacancies not only deviate the hole concentration (*p*) from the optimal level, but also act as carrier scattering centers to restrict the carrier mobility (μ_H)¹¹. Although the Ge vacancies can be efficiently suppressed by doping heavy elements such as Cd, Pb and Sb^{12–14}, which helps to optimize *p*, the *PF* only ranges from 16–37 $\mu\text{Wcm}^{-1}\text{K}^{-2}$, primarily assigned to degraded μ_H due to increased alloying scattering. Such low μ_H inevitably delays the response speed of TE materials, presenting a significant obstacle to their commercial viability¹⁵. While doping with Ge or Cu helps to enhance μ_H by discouraging carrier scattering via occupying Ge vacancies or providing additional carrier transport channels^{16–19}, yielding a high *ZT* value up to ~2.4 at 640 K, this approach is still heavily restricted by the solubility limit of dopants and the formation energy of point defects.

To address these concerns, a promising solution centers on developing rhombohedral GeTe with superior TE performance, particularly below the phase transition temperature, thereby establishing a groundwork for future development of efficient TE legs that eliminate the need for segmented architectures. Motivated by the exceptional efficacy of nanoparticles in optimizing electrical and thermal transport in typical TE systems, such as Bi₂Te₃, Mg₃Sb₂, Cu₂Se, etc.,^{20–23}, we seek to explore the specific interplay between heterogeneous interfaces and TE performance in rhombohedral GeTe from a nanocomposite perspective. Previously, we incorporated B inclusions into the GeTe matrix²⁴, with the aim of promoting the energy filtering effect to increase *S* and the formation of high-density dislocations to enhance phonon scattering. Unfortunately, this approach degraded the carrier mobility, which restricted further *ZT* enhancement. Herein, we find that direct incorporation of high-modulus nanoparticles into rhombohedral GeTe leads to a notable increase in μ_H despite increased interfacial potential barrier arising from a large grain boundary density as well as unfavorable energy band bending, with huge thermal resistance (*R_t*) at heterogeneous interfaces. This work aims to provide a deep insight into these exotic transport behaviors.

It is found that the TE performance of rhombohedral Ge_{0.94}Bi_{0.05}Te (the optimal composition identified by our previous study²⁴) can be boosted by the addition of TiB₂ nanoparticles, and the underlying mechanism is shown in Fig. 1a. It is acknowledged that tuning the deformation potential (Ξ) presents a powerful means to achieve high μ_H in TE materials²⁵. Notably, different from the classic Ξ modulation enabled by symmetry improvement via chemical bond engineering²⁵, the atomic displacement associated with elastic deformation is confined by the nanoparticle-induced interfacial constraint effect; this also reduces the sensitivity of the changes in band structure to elastic deformation, thereby lowering equivalent Ξ and enhancing μ_H . Additionally, the resulting heterogeneous interfaces contribute to facilitating charge transfer, and introducing high-frequency lattice vibration modes that enhance phonon-phonon scattering (Fig. 1a). The quality factor *B*, severing as an important indicator to reflect the degree of carrier-phonon decoupling²⁶, was calculated using Supplementary Eq. (1), shown in Fig. 1b. The *ZT* value increases from 1.7 to 2.66 as *B* increases from 1.1 to 2.1 at 613 K, indicating that TiB₂ addition helps to decouple the carrier-phonon interaction. To intuitively

evaluate the thermoelectric properties without the interference of temperature, the figure of merit (*Z*) is presented in Fig. 1c. Clearly, the TiB₂-added sample (*x* = 0.1) exhibits a high *Z* of $4.4 \times 10^{-3}\text{K}^{-1}$ at 600 K, surpassing the values of most state-of-the-art works reported previously^{11,24,27–34}. In addition, our work also achieves an extraordinary average *ZT* of 1.29 in rhombohedral GeTe, comparable to the record-high value for the Ag/Sb/Pb/Bi alloyed GeTe (Fig. 1d)^{11,24,27–34}, showing considerable potential of our strategy in TE property optimization.

Results

The crystal structure and microstructure of the as-prepared samples were examined to probe the structure-property relationship. The X-ray diffraction (XRD) patterns (Supplementary Fig. 1) reveal that all peaks can be indexed to the rhombohedral phase of GeTe, in good agreement with the standard PDF reference (JCPDS card: # 47-1079); no discernible TiB₂ peaks were observed, due to the insufficient additive amount falling below the detection limit of the X-ray diffractor. The Rietveld refinement (Supplementary Fig. 2) was performed based on the XRD data (Supplementary Fig. 1) to obtain the average lattice parameters, and the results were summarized in Supplementary Table 1. It is apparent that the lattice parameters exhibit negligible variations with increasing *x*, indicating a limited impact of TiB₂ addition on the lattice structure. Interestingly, Williamson-Hall analysis reveals similar micro-strain levels (~0.5%) for compositions with *x* between 0 and 0.1 within the margin of uncertainties, yet a pronounced increase to ~0.8% is observed in the *x* = 0.2 sample (Supplementary Fig. 3); these results imply that excessive TiB₂ addition introduces severe local lattice distortions³⁵.

The scanning electron microscopy (SEM) images of fracture surfaces show tightly packed grains with low porosity for all samples (Supplementary Fig. 4), in accordance with the calculated relative density data (~97%) in Supplementary Fig. 5. Compared to the pristine sample, the average grain size is nearly halved with the incorporation of TiB₂ (Supplementary Fig. 4), which can be attributed to the pinning effect induced by secondary phases. However, it shows little dependence on the additive amount, remaining at a similar level across different compositions (*x* = 0.05–0.2). The chemical composition determined by the electronic probe mapping analysis (EPMA) is shown in Supplementary Fig. 6. The intensity of the Ti and B signals in the EMPA maps increases progressively with *x*, whereas the localized enrichment of Ti and B elements suggests a decrease in the dispersion homogeneity at higher addition levels. Concurrently, Ge precipitates are ubiquitously present for each sample, arising from the low Ge vacancy formation energy³⁶; this is a characteristic feature of GeTe-based thermoelectrics.

The scanning transmission electron microscopy (STEM) images provide a deeper understanding of nanostructures inside the as-prepared samples. In contrast to the pristine sample with micro-sized grains (Fig. 2a), Fig. 2b shows that the addition of TiB₂ results in a nanocrystalline structure where the grain boundaries are decorated with identifiable nanoinclusions. Figure 2c shows the detailed information about the nano feature in Fig. 2b. It is worth noting that, for the *x* = 0.1 sample, the nanoinclusion is half-surrounded by the matrix, accompanied by the presence of nanopores. The corresponding energy dispersive X-ray spectroscopy (EDX) maps (Fig. 2d–h, Supplementary Fig. 7) reveal that these nanoinclusions are enriched with Ti and B, but depleted with Ge, Te and Bi, which implies that TiB₂ appears as a secondary phase in the matrix, in accordance with the EMPA analysis result Supplementary Fig. 6). Atomically resolved high-angle annular dark-field (HAADF) STEM image (collected from the grain on the left side of Fig. 2c) of the matrix phase (Fig. 2i) displays an ordered atomic arrangement, which matches well with the crystal structure of rhombohedral GeTe along the [110] zone axis. The atomic columns with brighter and darker contrast are assigned to Te and Ge, respectively, evidenced by the overlaid results of atomic-level STEM EDX

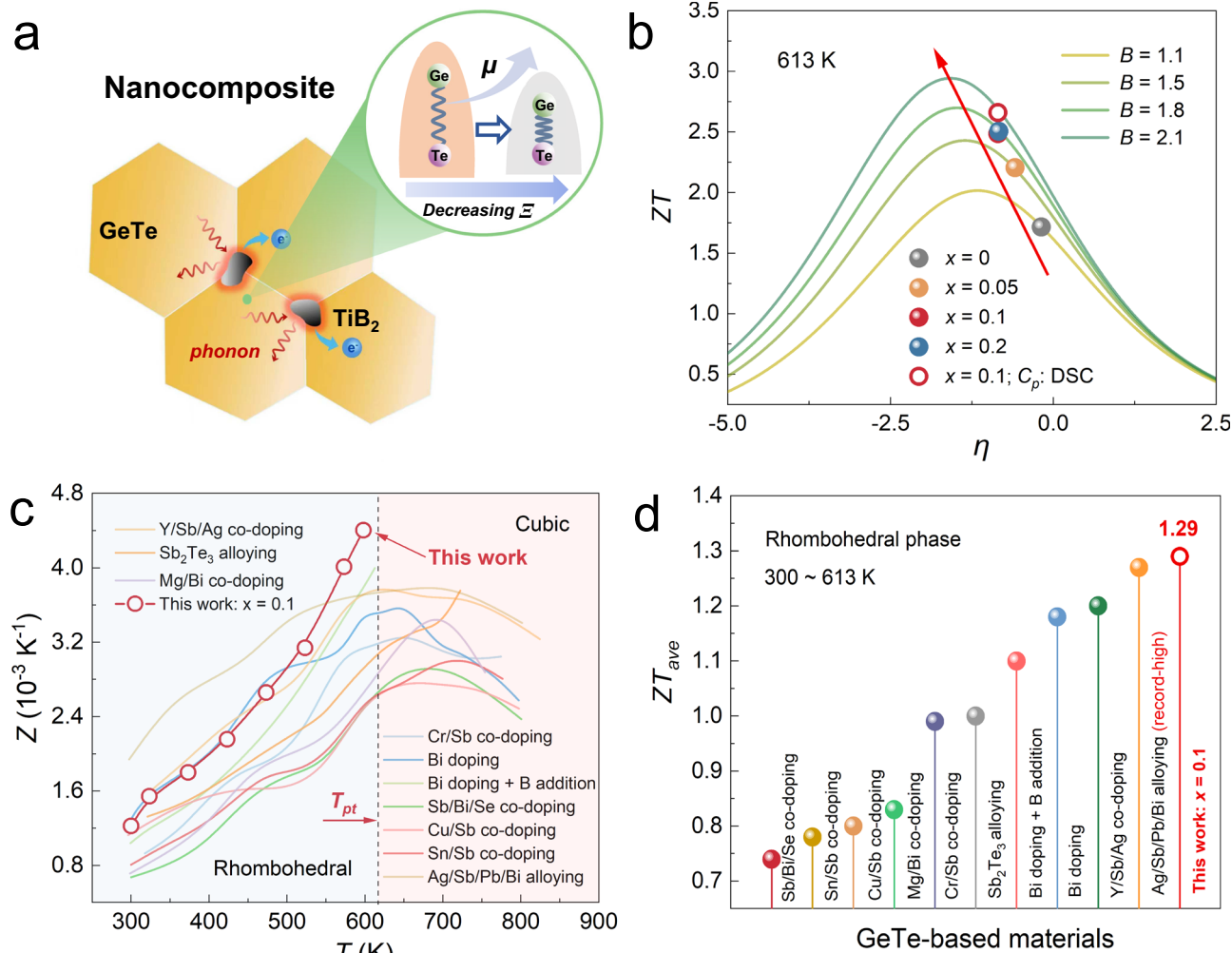


Fig. 1 | Nanocomposite strategy and enhanced thermoelectric figure of merits of GeTe-based materials. **a** Underlying mechanism of carrier-phonon decoupling in the composite. **b** ZT value as a function of reduced Fermi potential with different

quality factors at 613 K. **c** Comparison of Z values in this work with different GeTe-based thermoelectrics^{11,24,27–34}. (T_{pt} denotes the phase transition temperature). **d** Average ZT value contrast of various GeTe-based thermoelectrics^{11,24,27–34}.

maps (Supplementary Fig. 8); this is consistent with the site intensity of the HAADF image in Fig. 2j (the contrast is proportional to the square of atomic number Z^2). The separate elemental maps (Fig. 2i–l) show that the Bi atoms successfully enter the lattice of the GeTe matrix. Figure 2m shows the HAADF STEM images collected from the nanoinclusion, where two sets of lattice fringes can be observed. The corresponding line intensity maps and calculated plane spacing values are in good agreement with the (110) and (100) crystal planes (Fig. 2n, o) for the hexagonal TiB₂ with a space group of P 6/mmm (191), which is consistent with the crystal structure of the crystallographic information file (CIF) (number: ICSD190893). The presence of nano regions with distinct orientations demonstrates that this nanoinclusion constitutes a polycrystalline aggregate.

Figure 2p reveals the atomic structure of the interface between matrix phase and TiB₂ inclusions, highlighted by the red box in Fig. 2c. An incoherent phase boundary is observed, where the upper domain is GeTe phase along the [110] zone axis (confirmed by the top right inserted fast Fourier transform (FFT) pattern), and the bottom domain is TiB₂ secondary phase (confirmed by the bottom left inserted FFT pattern and plane spacing). Nevertheless, Fig. 2q shows one of the EDX line scan profiles in Supplementary Fig. 9 (line 1) across the interface; a sharp interface is observed in the absence of reaction layers, indicating that these two phases are immediately adjacent to each other. The quality of the interfacial contact seems sensitive to the additive

content. Notably, the interfacial adhesion deteriorates in the $x = 0.2$ sample, where some inclusions even exhibit minimal contact with pore edges (Supplementary Fig. 10). The strain analysis shows that the matrix near the interface accommodates strains through localized lattice distortions (Supplementary Fig. 11), in line with the Williamson-Hall analysis result (Supplementary Fig. 3). Furthermore, Supplementary Fig. 12 shows the elemental distribution of Ti and Te shows an overlap, which does not align with the natural interface morphology. When the electron beam is focused on the TiB₂ side (top right region in Supplementary Fig. 12i), two distinct sets of diffraction spots (blue circle: TiB₂; red circle: GeTe) appear in the FFT pattern (Supplementary Fig. 12j) corresponding to the region j in Supplementary Fig. 12i. Therefore, the thin edge of the TiB₂ grain is likely to extend over the GeTe grain, giving rise to a discontinuous interface.

The effects of TiB₂ addition on the electrical transport properties of Ge_{0.94}Bi_{0.05}Te were systematically investigated. As Fig. 3a shows, all samples exhibit a degenerate conduction behavior, as evidenced by the decrease in σ with increasing T . It is clear that σ can be efficiently reduced by the addition of TiB₂. Particularly, the room-temperature σ shows a gradual decrease from 3329.3 Scm⁻¹ to 2765.7 Scm⁻¹ as the additive content increases from 0 to 0.2 wt%. Meanwhile, the positive S values in Fig. 3b indicate that the electrical transport is dominated by holes. At 613 K, S increases from 216.0 μVK^{-1} to 261.6 μVK^{-1} with the TiB₂ content rising from 0 to 0.1 wt%, and remains almost constant

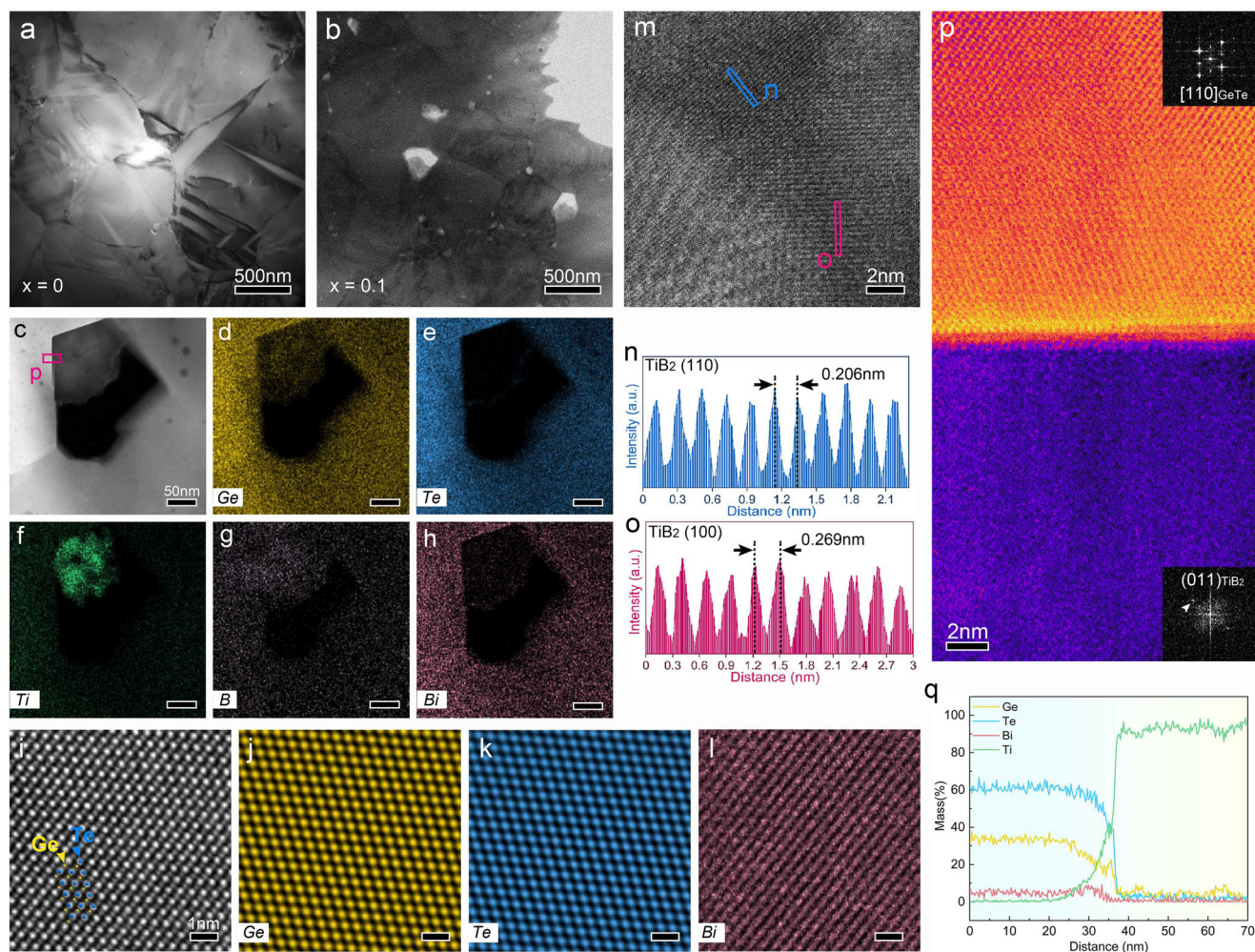


Fig. 2 | STEM analysis of the as-prepared $\text{Ge}_{0.94}\text{Bi}_{0.05}\text{Te} + x \text{ wt}\% \text{TiB}_2$ samples. **a** STEM image of the $x = 0$ sample. **b** STEM image of the $x = 0.1$ sample. **c** HAADF STEM image of the inclusion. **d–h** STEM EDX maps of Ge, Te, Ti, B and Bi corresponding to (c), respectively. **j** Atomically resolved HAADF STEM image of the matrix phase along the [110] zone axis. **i–l** Atomically resolved EDX maps

corresponding to (j). **m** Atomically resolved HAADF STEM image of the TiB_2 phase. **n, o** Intensity maps of (110) and (100) planes denoted by blue and red box in (m). **p** Atomically resolved HAADF STEM image and corresponding FFT patterns of the interface between the matrix and inclusion. **q** EDX line scan profile across the interface in the $x = 0.1$ sample.

when the additive content further increases up to 0.2 wt%. Consequently, a maximum PF of $50.1 \mu\text{Wcm}^{-1}\text{K}^{-2}$ is achieved in the $x = 0.1$ sample at 573 K (Fig. 3c), representing 19% enhancement compared to the pristine sample ($40.5 \mu\text{Wcm}^{-1}\text{K}^{-2}$ at 573 K). Similar to the variations of σ , the changes in κ follow a downward trend with increasing additive content (Fig. 3d); the value decreases from $3.2 \text{Wm}^{-1}\text{K}^{-1}$ for the $x = 0$ sample to $2.3 \text{Wm}^{-1}\text{K}^{-1}$ for the $x = 0.2$ sample at 300 K, showing a reduction of 28%.

As a result, the enhanced PF together with reduced κ yields a maximum ZT of -2.5 in both the $x = 0.1$ and $x = 0.2$ samples at 613 K (Fig. 3e), showing about 32% increase in comparison with the pristine sample ($ZT = 1.7$ at 613 K). The good reproducibility and repeatability of our experimental results are illustrated in Supplementary Figs. 13, 14, respectively. Notably, a maximum ZT of 2.66 can be even obtained at 613 K (Fig. 3e) when the specific heat capacity (C_p) determined by the differential scanning calorimetry (DSC) ($0.225 \text{Jg}^{-1}\text{K}^{-1}$; Supplementary Fig. 15) is used instead of the theoretical value derived from Dulong-Petit law ($0.241 \text{Jg}^{-1}\text{K}^{-1}$), very close to the record-high ZT reported by Jiang et al. for cubic GeTe-based thermoelectrics calculated using the same method ($ZT = 2.7$ at 750 K)³⁴. Such a giant enhancement in ZT below the phase transition temperature is of great significance for practical applications. Furthermore, a maximum quality factor B of 2.4 can be achieved at 600 K when the additive content increases up to

0.1 wt% (Fig. 3f), which is quite competitive among the GeTe-based materials reported in previous studies ($B = 0.4 - 2.5$)³⁷.

In order to better understand the electrical transport behavior of the as-prepared samples, carrier concentration (p) and mobility (μ_H) were measured at 300 K. As Fig. 4a shows, p decreases from $2.7 \times 10^{20} \text{cm}^{-3}$ to $2.1 \times 10^{20} \text{cm}^{-3}$ as x increases from 0 to 0.05, and then drops gradually to $1.9 \times 10^{20} \text{cm}^{-3}$ with x further increasing to 0.2; the corresponding μ_H exhibits an initial increase followed by a slight decline, reaching a maximum value of $96.9 \text{cm}^2 \text{V}^{-1} \text{s}^{-1}$ at $x = 0.1$. Figure 4b illustrates that the μ_H of this optimal composition exceeds the theoretical limit value calculated using the single parabolic band (SPB) model, which outperforms most GeTe-based thermoelectrics^{11,16,17,24,28,30,32,33,38}. Supplementary Fig. 16 presents the weighted mobility (μ_w) within the entire temperature range, calculated from Supplementary Eq. (2). The variation trend of μ_w with additive content (Supplementary Fig. 16) agrees well with that observed for μ_H at room temperature. Basically, the reduction in p should be ascribed to charge depletion at the heterogeneous interface; the electron transfer from TiB_2 into GeTe is encouraged, because the work function of GeTe matrix (-5.09eV) is higher than that of TiB_2 inclusions (-4.72eV)^{9,39,40}, as shown in Fig. 4c. The concept of electron donation from TiB_2 can also be supported by Ge $2p$ X-ray photoelectron spectrometer (XPS) spectra, where a peak shift toward lower binding

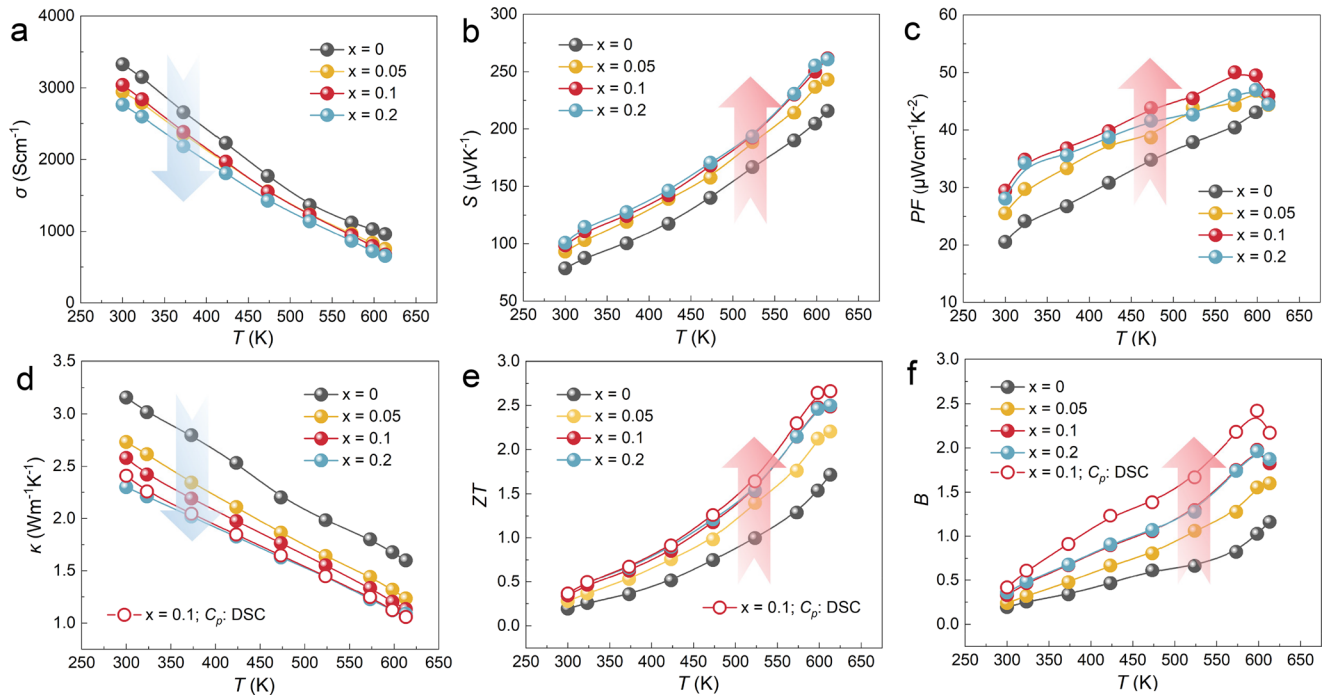


Fig. 3 | Thermoelectric properties of the as-prepared $\text{Ge}_{0.94}\text{Bi}_{0.05}\text{Te} + x \text{ wt}\% \text{TiB}_2$ samples. a Electrical conductivity. **b** Seebeck coefficient. **c** Power factor. **d** Thermal conductivity. **e** ZT values. **f** Quality factor B . The data calculated using the

differential scanning calorimetry (DSC) measured specific heat capacity (C_p) were represented by the hollow circular symbols.

energy can be observed after TiB_2 addition (Supplementary Fig. 17)⁴¹. Typically, an increase in the potential barrier would be anticipated, due to the band bending at the heterogeneous interface (Fig. 4c) along with increased grain boundary density (Supplementary Fig. 4), which is likely to deteriorate μ_H . The strains were also reported to make negligible contributions to modifying the band shape and hence the effective mass in rhombohedral GeTe⁴². Interestingly, the TiB_2 -added samples still show enhanced μ_H compared to the pristine sample, suggesting that additional regulatory factors are involved.

By plotting μ_H against T^{-1} , a linear relationship is presented below 473 K for all samples (Supplementary Fig. 18), indicative of acoustic phonon scattering as the dominating mechanism in degenerate semiconductors. Therefore, a scattering factor (r) of -0.5 was adopted to calculate the Pisarenko curve based on the SPB model using Supplementary Eq. (3–9) (Fig. 4d). It is found that all data points exactly fall onto the calculated curve, implying that the S values are primarily governed by p , with a fixed electronic density of state effective mass (m_d^*) of $1.72 m_e$. The carrier mobility can be evaluated using Eq. (1)⁴³:

$$\mu_H = \frac{(8\pi)^{0.5} \hbar^4 e C_L}{3m_d^{*2.5} (k_B T)^{1.5} \Xi^2} \quad (1)$$

where \hbar is the reduced Planck constant, C_L is the longitudinal elastic modulus, k_B is the Boltzmann constant, and Ξ is the deformation potential. Here, considering a fixed m_d^* for all samples, μ_H should be mainly determined by C_L and Ξ .

Figure 4e shows the C_L data of the as-prepared samples. Minimal TiB_2 addition (0.05–0.2 wt%) has already proven effective in enhancing C_L (red points). This enhancement results from both the phase mixing effect and load transfer effect, as reported by Liu et al. for composite materials⁴⁴. In view that the theoretical C_L , calculated using the volume mixture rule (blue points)⁴⁵, shows a slight increase from 70.3 GPa to 71.7 GPa with increasing x , the phase mixing effect does not take a dominating role. Thus, the difference between the experimental data and mixture rule data (pink region) should represent the

contribution from the load transfer effect, which could be understood through the inset in Fig. 4e and Eq. (2)⁴⁶:

$$\sigma_L = \varepsilon C_L \quad (2)$$

where σ_L and ε represent the longitudinal stress and strain, respectively. It is noted that the C_L of TiB_2 is $\sim 582 \text{ GPa}$ ⁴⁷, about eight times the value of GeTe (70.3 GPa)⁴⁸, demonstrating superior resistance to elastic deformation. Given an intimate contact between the inclusions and matrix material, the ε of the GeTe matrix would be constrained by TiB_2 particles ($\Delta\varepsilon$) when a tensile stress (σ_L) is applied, giving rise to a smaller elastic strain compared to the pristine GeTe. Similarly, TiB_2 can also act as a restraint against matrix contraction under compression. Consequently, effective load transfer from the matrix to the reinforcing phases is finalized when the coordinated elastic deformation is established at the interface, enabling the inclusions to bear a larger stress⁴⁹. The enhanced stiffness induced by TiB_2 particles is also echoed by the Young's modulus data measured by a nano indenter (Supplementary Fig. 19).

Figure 4f displays the mean free path of carriers (l_{car}) and relative deformation potential (Ξ/Ξ_0) calculated using Supplementary Eqs. (10–12). It is evident that l_{car} shows an increase followed by a decline, peaking at $x = 0.1$; this variation trend matches well with changes in μ_H , but is opposite to that of Ξ/Ξ_0 . According to the Bardeen-Shockley theory⁵⁰, the thermal vibrations can lead to the dilation or shrinkage of crystal lattices and hence the changes in electronic band energy. The shifts of energy band boundaries with elastic deformation are therefore defined as Ξ , acting as an indicator to reflect the intensity of carrier-phonon coupling⁵¹. Previous investigations mainly focus on minimizing intrinsic Ξ by improving the symmetry structure via proper elemental doping⁴³. Herein, our work, despite methodological differences, converges on a similar advantage. Although the XRD Rietveld refinement results (Supplementary Fig. 2, Supplementary Table 1) show that the atomic positions and angles are not significantly altered after TiB_2 addition, indicative of

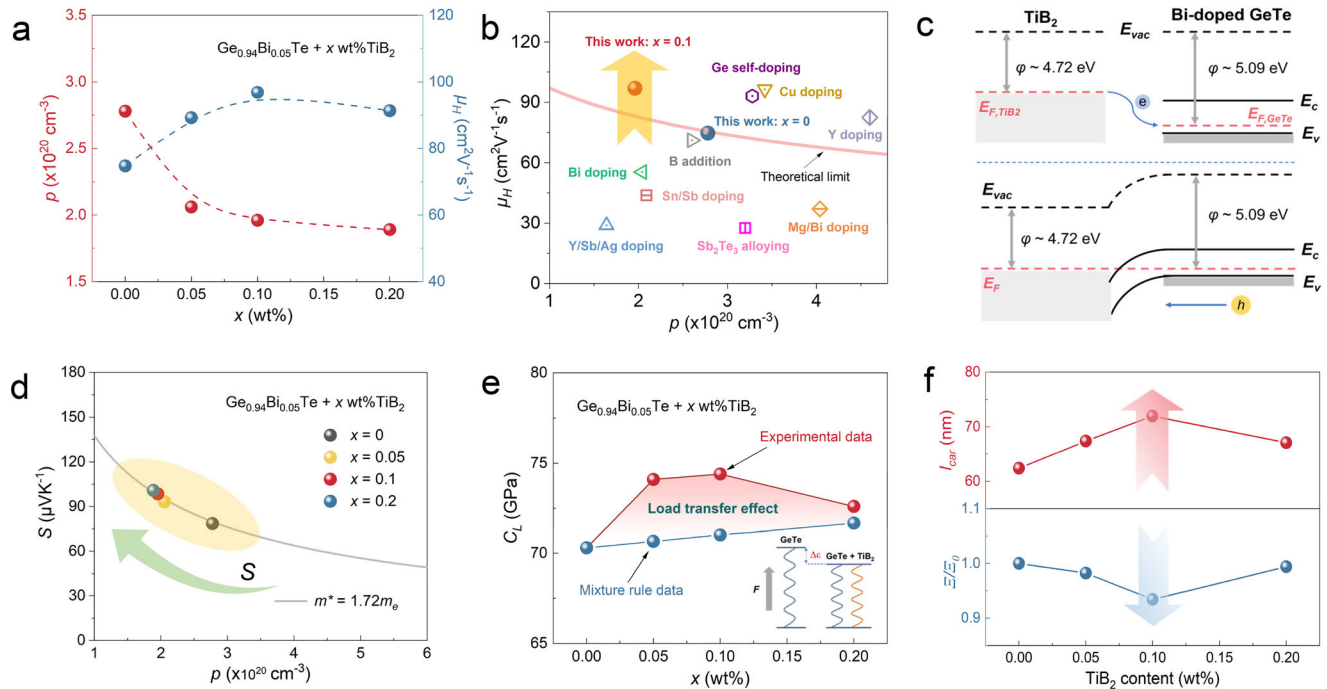


Fig. 4 | Electrical transport analysis for the as-prepared $\text{Ge}_{0.94}\text{Bi}_{0.05}\text{Te} + x \text{ wt}\% \text{TiB}_2$ samples. a Carrier concentration and mobility. **b** Comparison of carrier mobility in this work with different GeTe-based thermoelectrics^{11,16,17,24,28,30,32,33,38} (The theoretical limit is calculated using the single parabolic band model at 300 K). **c** Schematic of the interfacial band structure before and after contact. **d** Seebeck

coefficient plot against carrier concentration based on the SPB model at 300 K. **e** Longitudinal elastic modulus derived from the sound velocity method and the mixture rule (The pink region represents the contribution from the load transfer effect, and the inset describes the interfacial constraint effect). **f** Calculated mean free path of carriers and relative deformation potential.

unchanged intrinsic Ξ , the thermal vibration-induced elastic deformation can be efficiently weakened by the interfacial constraint effect, thereby limiting the actual shifts of energy band boundaries of the matrix material. In essence, this result can be alternatively understood as a reduction in the equivalent Ξ that leads to enhanced μ_H .

Owing to the difference in thermal expansion coefficients (TEC) between GeTe ($5.60 \times 10^{-5} \text{ K}^{-1}$ between 296 - 648 K) and TiB_2 ($2.37 \times 10^{-5} \text{ K}^{-1}$ between 250 - 900 K)^{24,52}, the misfit strains (ε_m) can be generated according to Eshelby's inclusion model (Eq. (3))⁵³:

$$\varepsilon_m = (\alpha_m - \alpha_i)\Delta T \quad (3)$$

where α_m and α_i denote the TEC of the matrix and inclusions, respectively, and ΔT is the temperature difference. Because the TEC of GeTe is greater than that of TiB_2 , GeTe is subjected to a large tensile stress during the cooling stage. A simplified two-phase model was employed to perform a preliminary finite element analysis of the stress distribution in the sintered composite, serving as theoretical evidence for stress at the interfaces (Supplementary Fig. 20, Supplementary Table 2). It is inferred that the 'void-particle' structure in Fig. 2c may be a natural consequence of differential contraction between the matrix and the secondary phases. To offset the increased surface energy caused by pore formation, the secondary phase tends to resist separation from the matrix on one facet to keep a low-energy state⁵⁴. As x further increases up to 0.2, obvious aggregation of TiB_2 nanoparticles can be formed, which is likely to induce severe stress concentrations⁵⁵. The interfacial debonding (Supplementary Fig. 10) may occur with the stress exceeding the elastic limit to trigger lattice distortions (Supplementary Fig. 11). The complex interface presented in Supplementary Fig. 12 is likely a direct manifestation of stress levels exceeding the critical threshold. Because the severe lattice distortions and deteriorated interfacial contacts can lead to partial failure of the load transfer effect, a small decline in C_L and a recovery in Ξ/Ξ_0 are revealed.

In order to unveil the origin of reduced κ in the TiB_2 -added samples, the electronic (κ_e) and lattice (κ_L) contributions were clarified. As expected, κ_e exhibits a trend which mirrors that of σ (Fig. 5a), as it is strongly influenced by the latter. Notably, TiB_2 addition proves effective in lowering κ_L . By incorporating 0.2 wt% TiB_2 into the matrix, κ_L is reduced from $1.15 \text{ W m}^{-1} \text{ K}^{-1}$ to $0.71 \text{ W m}^{-1} \text{ K}^{-1}$ at 300 K, showing a reduction of 38% (Fig. 5b). The significantly reduced κ_L in combination with the enhanced μ_w yields a maximum μ_w/κ_L ratio of ~600 for both the $x = 0.1$ and $x = 0.2$ samples (Supplementary Fig. 21), reflecting a dramatic net gain between electrical and thermal transport. Such high μ_w/κ_L ratios indicate that proper TiB_2 addition can enhance phonon scattering without degrading carrier transport; this effective carrier-phonon decoupling is mainly responsible for the increased B in Fig. 3f.

To further identify the primary factors influencing κ_L , the average sound velocity (v_{ave}) was derived from the data in Supplementary Table 3 based on Supplementary Eq. (13), and the mean phonon free path (l_p) at room temperature was calculated using Supplementary Eq. (14). As shown in Fig. 5c, despite a nearly constant v_{ave} across all samples, a gradual reduction in l_p occurs with increasing x , indicating that the intensity of phonon scattering is positively correlated with TiB_2 content. The κ_L data were fitted by the Debye-Callaway model using Supplementary Eqs. (15–20) to examine the differences between experimental and simulation results (Fig. 5d)⁵⁶, based on the physical parameters listed in Supplementary Table 4. For the $x = 0$ sample, the simulated κ_L basically match with the experimental κ_L , with the contributions from Umklapp process scattering, grain boundary scattering and point defect scattering taken into account. In contrast, a marked discrepancy persists between the experimental and simulated values for the $x = 0.1$ sample, even after incorporating the additional contributions from nanoparticle scattering. Given that l_p ranges from 0.7 to 1.1 nm, much shorter than the size of TiB_2 nano-inclusions (300 - 500 nm), the scattering effect induced by heterogeneous interfaces should prevail over the size effect, which is overlooked in

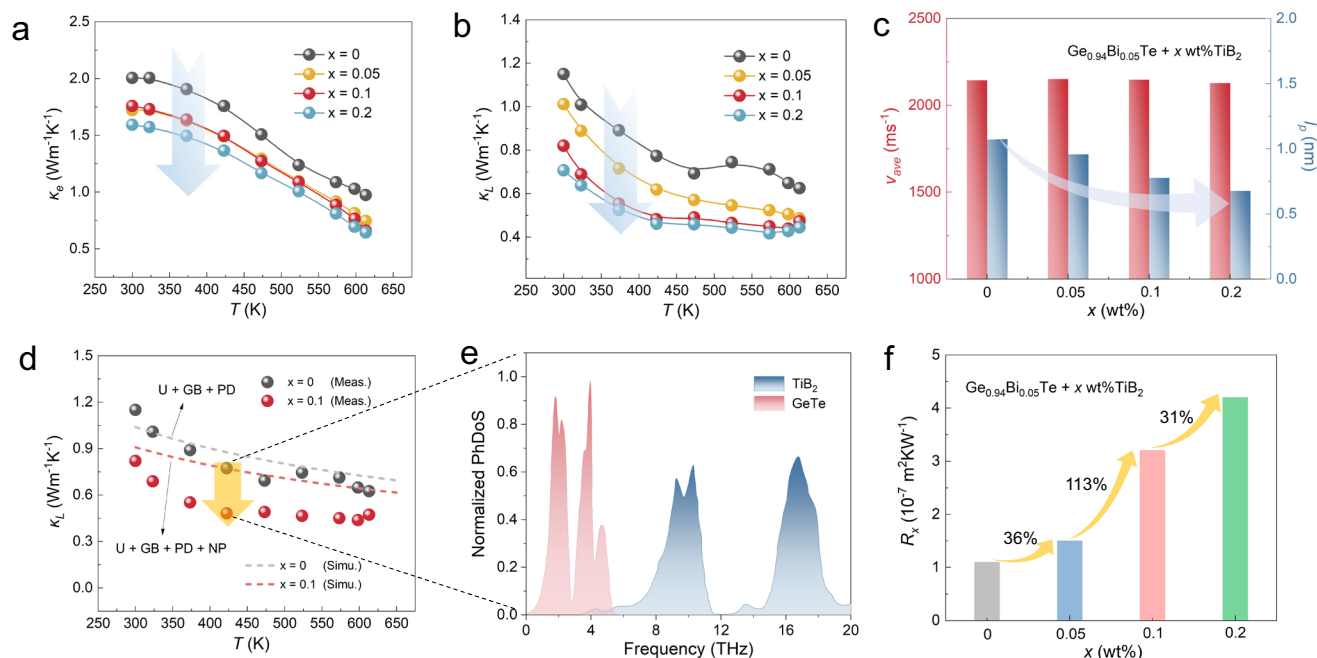


Fig. 5 | Thermal transport analysis for the as-prepared $\text{Ge}_{0.94}\text{Bi}_{0.05}\text{Te} + x \text{ wt}\% \text{TiB}_2$ samples. a Electronic thermal conductivity. **b** Lattice thermal conductivity. **c** Calculated average sound velocity and mean free path of phonons. **d** Differences between the experimental lattice thermal conductivity and simulated thermal conductivity derived from Debye-Callaway model (U: Umklapp process scattering;

GB: grain boundary scattering; PD: point defect scattering; NP: nanoparticle scattering). **e** Comparison of phonon density of states in GeTe and TiB_2 ; data for this figure are derived from earlier studies^{58,59}. **f** The calculated interfacial thermal resistance of the as-prepared samples (The yellow arrow denotes the percentage increase).

the theoretical model. On one hand, the atomic displacement is confined due to the interfacial constraint effect, leading to an increased effective force constant F and hence a higher frequency ω , according to Eq. (4)⁵⁷:

$$\omega = 2\sqrt{\frac{F}{M}} \sin\left(\frac{\pi k}{2k_c}\right) \quad (4)$$

where F is the force constant, M is the atomic mass, k is the wave vector magnitude, and k_c is the cut-off wave vector magnitude. On the other hand, the phonon density of states (PhDoS) of GeTe and TiB_2 are mainly distributed within the frequency range of 0–5.5 THz and 3.8–20 THz, respectively, showing a limited overlap region (Fig. 5e)^{58,59}.

Therefore, the addition of TiB_2 nanoparticles can induce high-frequency vibration modes near the interface; the resulting high-energy phonons can effectively scatter low-energy phonons, thereby generating huge interfacial thermal resistance (R_x)⁶⁰. The R_x of the as-prepared composites can be roughly estimated using Supplementary Eq. (21), and the calculation results were summarized in Fig. 5f. As expected, a large R_x of $3.2 \times 10^{-7} \text{ m}^2 \text{KW}^{-1}$ is generated after the addition of 0.1 wt% TiB_2 . Despite a doubling in TiB_2 content (0.2 wt%), the R_x increases by a smaller margin, which could be attributed to the limited effective contact area of TiB_2 nano-inclusions due to severe aggregations.

Discussion

In summary, we reveal the role of TiB_2 nano-inclusions in synergistically optimizing the electrical and thermal transports in rhombohedral $\text{Ge}_{0.94}\text{Bi}_{0.05}\text{Te}$. After 0.1 wt% TiB_2 addition, the degree of elastic deformation is efficiently weakened through the interfacial constraint effect, limiting the actual shifts of energy band boundaries of the matrix and thus decreasing the equivalent deformation potential. The carrier mobility is therefore enhanced due to efficient carrier-phonon decoupling. In addition, the presence of heterogeneous interfaces contributes not only to reducing carrier concentration via charge

depletion, but also to generating huge thermal resistance mainly due to the mismatched phonon density of states and residual stress at the interface. Thanks to 19% enhancement in power factor and 28% reduction in thermal conductivity compared to the pristine sample, a superior ZT of 2.66 is yielded at 613 K. Furthermore, a high average ZT of 1.29 is obtained between 300 and 613 K, representing a noticeable advance in wide-temperature-range TE performance of rhombohedral GeTe. Our work helps to boost the ZT values of rhombohedral GeTe below the phase transition temperature and provides different insights into the modulation of deformation potential and the origin of low thermal conductivity.

Methods

Synthesis

Raw materials of Ge (powders, 99.999%), Te (powders, 99.999%) and Bi (powders, 99.99%), weighted according to the optimal matrix composition ($\text{Ge}_{0.94}\text{Bi}_{0.05}\text{Te}$), were first sealed in tungsten carbide jars under an Ar atmosphere, followed by high-energy planetary milling at 450 rpm for 12 h. Subsequently, different mass ratios of TiB_2 (powders, 99.9%) were added into the mixture based on the nominal compositions ($\text{Ge}_{0.94}\text{Bi}_{0.05}\text{Te} + x \text{ wt}\%$, $x = 0, 0.05, 0.1$ and 0.2), after which the combined powders are subjected to planetary milling at 300 rpm for 3 h. Finally, different batches of resulting powders were sintered at 873 K for 5 min under an axial pressure of 60 MPa in a vacuum of 5 Pascal, using a spark plasma sintering furnace (SPS 211Lx, Fuji Electronic, Japan).

Characterization

The phase identification was carried out by an X-ray diffractometer with a $\text{Cu K}\alpha$ source (D8 ADVANCE, Bruker, Germany; $\lambda = 1.5418 \text{ \AA}$). The Rietveld refinement was performed using the Topas software. The internal lattice strain was estimated by the Williamson-Hall method. The morphology and microstructure of fracture surfaces were determined by a field-emission scanning electron microscope (FESEM, Zeiss Merlin, Germany). The average grain size was evaluated using the

linear intercept method. The chemical composition was examined by an electron probe micro analyzer (EPMA, JXA-8230, JEOL, Japan). STEM characterization was conducted by a JEOL JEM-ARM300F2 GRAND ARMTM2 aberration-corrected STEM, operated at 300 kV.

Transport property measurement

The electrical conductivity (σ) and Seebeck coefficient (S) were recorded by a transport property measurement system (ZEM-3, ADVANCE RIKO, Japan) under low-pressure He atmosphere. The total thermal conductivity (κ) was calculated from the equation $\kappa = \rho DC_p$, where ρ is the bulk density obtained by the Archimedes' method, D is the diffusivity measured by a laser flash instrument (LFA457, Netzsch, Germany), and C_p is the specific heat capacity determined by both the Dulong-Petit law and DSC (STA 449 F3, Jupiter, Netzsch, Germany). The electronic thermal conductivity (κ_e) was calculated from the equation $\kappa_e = L\sigma T$, where L represents the Lorenz factor estimated by the single parabolic band model, σ is the measured electrical conductivity, and T is the absolute temperature. The lattice thermal conductivity (κ_L) was derived from the equation $\kappa_L = \kappa - \kappa_e$. Both the electrical and thermal transport data were collected perpendicular to the axial SPS pressure. The longitudinal and transversal sound velocities were determined by the ultrasonic probing method. The carrier concentration and mobility were determined by a Hall measurement system (ResiTest 8340DC, Toyo, Japan).

Mechanical property measurement

The longitudinal elasticity modulus (C_L) was calculated from the equation $C_L = \rho v_L^2$, where ρ is the bulk density, and v_L is the longitudinal sound velocity. The Young's modulus and microhardness were determined by a nano indenter (Nano Indenter G200, China) at room temperature in air.

Data availability

The data generated in this study are provided in the Supplementary Information/Source Data file. Source data are provided with this paper.

References

- Qin, Y. et al. Grid-plainification enables medium-temperature PbSe thermoelectrics to cool better than Bi₂Te₃. *Science* **383**, 1204–1209 (2024).
- Hu, H. et al. Chemical bond engineering toward extraordinary power factor and service stability in thermoelectric copper selenide. *Joule* **8**, 416–429 (2024).
- Sales, B. C. Electron crystals and phonon glasses: a new path to improved thermoelectric materials. *MRS Bull.* **23**, 15–21 (1998).
- Zhuang, H.-L., Yu, J. & Li, J.-F. Nanocomposite strategy toward enhanced thermoelectric performance in bismuth telluride. *Small Sci.* **5**, 2400284 (2024).
- Zhang, X. et al. GeTe thermoelectrics. *Joule* **4**, 986–1003 (2020).
- Zhu, Y. et al. Large mobility enables higher thermoelectric cooling and power generation performance in n-type AgPb_{18+x}SbTe₂₀ crystals. *J. Am. Chem. Soc.* **145**, 24931–24939 (2023).
- Li, J. et al. Electronic origin of the high thermoelectric performance of GeTe among the p-type group IV monotelellurides. *NPG Asia Mater.* **9**, e353–e353 (2017).
- Li, J. et al. Low-symmetry rhombohedral GeTe thermoelectrics. *Joule* **2**, 976–987 (2018).
- Pei, J. et al. Design and fabrication of segmented GeTe/(Bi, Sb)₂Te₃ thermoelectric module with enhanced conversion efficiency. *Adv. Funct. Mater.* **33**, 2214771 (2023).
- Cao, J. et al. Designing a good compatibility factor in segmented Bi_{0.5}Sb_{1.5}Te₃-GeTe thermoelectrics for high power conversion efficiency. *Nano Energy* **96**, 107147 (2022).
- Jiang, Y. et al. Evolution of defect structures leading to high ZT in GeTe-based thermoelectric materials. *Nat. Commun.* **13**, 6087 (2022).
- Hong, M. et al. Arrays of planar vacancies in superior thermoelectric Ge_{1-x-y}Cd_xBi_yTe with band convergence. *Adv. Energy Mater.* **8**, 1801837 (2018).
- Nshimiyimana, E. et al. Realization of a non-equilibrium process for high thermoelectric performance Sb-doped GeTe. *Sci. Bull.* **63**, 717–725 (2018).
- Feng, Y. et al. Band convergence and carrier-density fine-tuning as the electronic origin of high-average thermoelectric performance in Pb-doped GeTe-based alloys. *J. Mater. Chem. A* **8**, 11370–11380 (2020).
- Qin, B. & Zhao, L.-D. Moving fast makes for better cooling. *Science* **378**, 832–833 (2022).
- Dong, J. et al. Medium-temperature thermoelectric GeTe: vacancy suppression and band structure engineering leading to high performance. *Energy Environ. Sci.* **12**, 1396–1403 (2019).
- Bu, Z. et al. Dilute Cu₂Te-alloying enables extraordinary performance of r-GeTe thermoelectrics. *Mater. Today Phys.* **9**, 100096 (2019).
- Yin, L.-C. et al. Interstitial Cu: an effective strategy for high carrier mobility and high thermoelectric performance in GeTe. *Adv. Funct. Mater.* **33**, 2301750 (2023).
- Li, H. et al. Cu-enhanced thermoelectric performance in GeTe by synchronous modulation of hole concentration and thermal conductivity. *Matter* **9**, 102609 (2026).
- Zhuang, H.-L. et al. Strong and efficient bismuth telluride-based thermoelectrics for Peltier microcoolers. *Natl. Sci. Rev.* **11**, nwae329 (2024).
- Li, J.-W. et al. In situ engineering of grain boundary phase toward superior thermoelectric performance in Mg₃(Sb, Bi)₂. *Adv. Mater.* **37**, 2503665 (2025).
- Yu, J. et al. Ultralow thermal conductivity and high ZT of Cu₂Se-based thermoelectric materials mediated by TiO_{2-n} nanoclusters. *Joule* **8**, 2652–2666 (2024).
- Liu, X. et al. Enhancing the thermoelectric properties of TiO₂-based ceramics through addition of carbon black and graphene oxide. *Carbon* **216**, 118509 (2024).
- Jiang, Y. et al. Exceptional figure of merit achieved in boron-dispersed GeTe-based thermoelectric composites. *Nat. Commun.* **15**, 5915 (2024).
- Gao, T. et al. Extending the temperature range of the Cmcm phase of SnSe for high thermoelectric performance. *Science* **390**, 1266–1271 (2025).
- Yin, Z. et al. Phase boundary metallization enables electron-phonon transport decoupling in PbS-based thermoelectric. *Adv. Funct. Mater.* <https://doi.org/10.1002/adfm.202515932> (2025).
- Xing, T. et al. High efficiency GeTe-based materials and modules for thermoelectric power generation. *Energy Environ. Sci.* **14**, 995–1003 (2021).
- Hong, M. et al. Rashba effect maximizes the thermoelectric performance of GeTe derivatives. *Joule* **4**, 2030–2043 (2020).
- Xie, L. et al. Lead-free and scalable GeTe-based thermoelectric module with an efficiency of 12%. *Sci. Adv.* **9**, eadg7919 (2025).
- Xing, T. et al. Ultralow lattice thermal conductivity and superhigh thermoelectric figure-of-merit in (Mg, Bi) co-doped GeTe. *Adv. Mater.* **33**, 2008773 (2021).
- Hong, M. et al. Computer-aided design of high-efficiency GeTe-based thermoelectric devices. *Energy Environ. Sci.* **13**, 1856–1864 (2020).
- Tsai, Y.-F. et al. Compositional fluctuations locked by athermal transformation yielding high thermoelectric performance in GeTe. *Adv. Mater.* **33**, 2005612 (2021).
- Liu, C. et al. Charge transfer engineering to achieve extraordinary power generation in GeTe-based thermoelectric materials. *Sci. Adv.* **9**, eadh0713 (2025).
- Jiang, B. et al. High figure-of-merit and power generation in high-entropy GeTe-based thermoelectrics. *Science* **377**, 208–213 (2022).

35. Hanus, R. et al. Lattice softening significantly reduces thermal conductivity and leads to high thermoelectric efficiency. *Adv. Mater.* **31**, 1900108 (2019).
36. Li, M., Shi, X.-L. & Chen, Z.-G. Trends in GeTe thermoelectrics: from fundamentals to applications. *Adv. Funct. Mater.* **34**, 2403498 (2024).
37. Jiang, Y., Yu, J., Li, H., Zhuang, H.-L. & Li, J.-F. Chemical modulation and defect engineering in high-performance GeTe-based thermoelectrics. *Chem. Sci.* **16**, 1617–1651 (2025).
38. Gao, W. et al. Improved thermoelectric performance of GeTe via efficient yttrium doping. *Appl. Phys. Lett.* **118**, 33901 (2021).
39. Wang, Q. et al. First-principles study on the stability and work function of low-index surfaces of TiB_2 . *Comput. Mater. Sci.* **172**, 109356 (2020).
40. Yang, D. et al. Blocking ion migration stabilizes the high thermoelectric performance in Cu_2Se composites. *Adv. Mater.* **32**, 2003730 (2020).
41. Zhao, W. et al. Superparamagnetic enhancement of thermoelectric performance. *Nature* **549**, 247–251 (2017).
42. Yan, S. & Gong, J. Impact of uniaxial strain on the electronic and transport properties of monolayer α -GeTe. *Nanotechnology* **31**, 445706 (2020).
43. Shi, H. et al. Realizing high in-plane carrier mobility in n-type SnSe crystals through deformation potential modification. *Energy Environ. Sci.* **16**, 3128–3136 (2023).
44. Liu, Y. Q., Cong, H. T., Wang, W., Sun, C. H. & Cheng, H. M. AlN nanoparticle-reinforced nanocrystalline Al matrix composites: fabrication and mechanical properties. *Mater. Sci. Eng. A* **505**, 151–156 (2009).
45. Bedolla, E., Lemus-Ruiz, J. & Contreras, A. Synthesis and characterization of Mg-AZ91/AlN composites. *Mater. Des.* **38**, 91–98 (2012).
46. Timoshenko, S. P. & Kaneta, G. K. Timoshenko theory of elasticity. (1973).
47. Waśkowska, A. et al. Thermoelastic properties of ScB_2 , TiB_2 , YB_4 and HoB_4 : Experimental and theoretical studies. *Acta Mater.* **59**, 4886–4894 (2011).
48. Suwardi, A. et al. Tailoring the phase transition temperature to achieve high-performance cubic GeTe-based thermoelectrics. *J. Mater. Chem. A* **8**, 18880–18890 (2020).
49. Suo, Y. et al. Investigation on the mechanism of the load transfer behavior in particle-reinforced metal matrix composites. *J. Mater. Res.* **40**, 250–264 (2025).
50. Bardeen, J. & Shockley, W. Deformation potentials and mobilities in non-polar crystals. *Phys. Rev.* **80**, 72–80 (1950).
51. Wang, H., Pei, Y., LaLonde, A. D. & Snyder, G. J. Weak electron-phonon coupling contributing to high thermoelectric performance in n-type PbSe. *Proc. Natl. Acad. Sci.* **109**, 9705–9709 (2012).
52. Özkan, H. Temperature dependence of the isothermal bulk modulus of TiB_2 . *Intermetallics* **19**, 596–598 (2011).
53. Majumdar, S., Kupperman, D. & Sing, J. Determinations of residual thermal stresses in a $\text{SiC-Al}_2\text{O}_3$ composite using neutron diffraction. *J. Am. Ceram. Soc.* **71**, 858–863 (1988).
54. Overbury, S. H., Bertrand, P. A. & Somorjai, G. A. Surface composition of binary systems. Prediction of surface phase diagrams of solid solutions. *Chem. Rev.* **75**, 547–560 (1975).
55. Romanov, V. S., Lomov, S. V., Verpoest, I. & Gorbatiikh, L. Stress magnification due to carbon nanotube agglomeration in composites. *Compos. Struct.* **133**, 246–256 (2015).
56. Zhu, Y.-K. et al. General design of high-performance and textured layered thermoelectric materials via stacking of mechanically exfoliated crystals. *Joule* **8**, 2412–2424 (2024).
57. Wu, Y. et al. Lattice strain advances thermoelectrics. *Joule* **3**, 1276–1288 (2019).
58. Deligoz, E., Colakoglu, K. & Ciftci, Y. O. Lattice dynamical properties of ScB_2 , TiB_2 , and VB_2 compounds. *Solid State Commun.* **149**, 1843–1848 (2009).
59. Dangić, Đ., Murphy, A. R., Murray, É D., Fahy, S. & Savić, I. Coupling between acoustic and soft transverse optical phonons leads to negative thermal expansion of GeTe near the ferroelectric phase transition. *Phys. Rev. B* **97**, 224106 (2018).
60. Zhou, Z. et al. Compositing effects for high thermoelectric performance of Cu_2Se -based materials. *Nat. Commun.* **14**, 2410 (2023).

Acknowledgments

This work was supported by the National Key R&D Program of China (2025YFF0524500 to Y.P.), National Natural Science Foundation of China (52502275 to J.C.Y.; 52401263 to Y.P.) and the Fundamental Research Funds for the Central University (2024CDJQYJCYJ-001 to J.C.Y.).

Author contributions

J.-F.L. and X.Y.Z. contributed to the project supervision. Y.P. and J.C.Y. were responsible for the funding acquisition. J.C.Y. and Y.L.J. initiated the idea and drafted the manuscript. J.C.Y., X.D.L., and Y.L.J. designed the experiment and conducted principal investigations. C.C., J.-W.L., H.H.H., and L.S. helped to analyze the experimental data. T.X., B.-B.R., and G.Y.W. provided helpful discussions. B.L.M., Y.P., X.Y.Z., and J.-F.L. secured the experimental resources. All authors co-edited the manuscript.

Competing interests

The authors declare no competing interests.

Additional information

Supplementary information The online version contains supplementary material available at <https://doi.org/10.1038/s41467-026-70793-6>.

Correspondence and requests for materials should be addressed to Yilin Jiang, Yu Pan, Xiaoyuan Zhou or Jing-Feng Li.

Peer review information *Nature Communications* thanks Michihiro Ohta, Bhuvanesh Srinivasan and the other anonymous reviewer(s) for their contribution to the peer review of this work. A peer review file is available.

Reprints and permissions information is available at <http://www.nature.com/reprints>

Publisher's note Springer Nature remains neutral with regard to jurisdictional claims in published maps and institutional affiliations.

Open Access This article is licensed under a Creative Commons Attribution-NonCommercial-NoDerivatives 4.0 International License, which permits any non-commercial use, sharing, distribution and reproduction in any medium or format, as long as you give appropriate credit to the original author(s) and the source, provide a link to the Creative Commons licence, and indicate if you modified the licensed material. You do not have permission under this licence to share adapted material derived from this article or parts of it. The images or other third party material in this article are included in the article's Creative Commons licence, unless indicated otherwise in a credit line to the material. If material is not included in the article's Creative Commons licence and your intended use is not permitted by statutory regulation or exceeds the permitted use, you will need to obtain permission directly from the copyright holder. To view a copy of this licence, visit <http://creativecommons.org/licenses/by-nc-nd/4.0/>.

© The Author(s) 2026